ChemComm

COMMUNICATION

View Article Online
View Journal | View Issue

Cite this: *Chem. Commun.*, 2024, **60**, 13219

Received 16th September 2024,
Accepted 17th October 2024

DOI: 10.1039/d4cc04773g

rsc.li/chemcomm

Lattice expansion of MnO induced by sulphur doping for enhanced aqueous zinc-ion diffusion and storage†

Zixiang Cui,[a] Luwei Shi,[a] Yan Lin,[b] Shiliu Yang,[c] Zhengyi Wu,[a] Tao Hu,[b] Ulla Lassi *[b] and Ruguang Ma *[a]

Lattice engineering is reported to enhance Zn^{2+} storage capability of MnO *via* anionic doping, which effectively lowers the Zn^{2+} diffusion barrier and boosts Zn^{2+} diffusion kinetics. The optimized $MnOS_{0.3}$@rGO exhibits superior rate capability and reversible capacity of 115.1 mA h g^{-1} at 0.5 A g^{-1} for 350 cycles.

In recent years, aqueous zinc-ion batteries (ZIBs) have emerged as a promising candidate for next-generation energy storage systems due to their high energy density, low cost, and environmental friendliness.[1] However, the slow kinetics of zinc ions (Zn^{2+}) during charge–discharge processes has been a major challenge limiting the rate capability and high-power performance of ZIBs.[2,3] To address this issue, various strategies have been explored, including the design of novel electrode materials and the optimization of electrolyte composition.[4]

Manganese-based materials are widely applied as cathode materials in ZIBs due to their high theoretical capacity, abundant availability, and relatively low cost.[5] However, the application of manganese-based materials in ZIBs faces some challenges.[6,7] Additionally, structural changes may occur during charge–discharge cycles, leading to capacity fading and reduced cycling stability.[8] To overcome these challenges, researchers have been exploring various strategies to improve the electrochemical performance of manganese-based materials.[9,10] For instance, nanostructure design, doping with other elements, and composites with conductive materials have been attempted to enhance the conductivity and structural stability of manganese-based materials.[11]

In recent years, researchers have made certain progress on MnO-based materials. A typical example is that Tang *et al.* reported the application of metal–organic framework (MOF)-derived manganese oxide (MnO) composites with active functional groups in aqueous ZIBs.[12] Moreover, Shen *et al.* added multi-wall carbon nanotubes (MWCNTs) to form 3D ternary MnO/rGO/MWCNTs (MPGC) with a high specific capacity of 267.4 mA h g^{-1} at 0.2 A g^{-1} and good stability with retention rate of 96.2% after 200 cycles at 0.5 A g^{-1}.[13]

Among these strategies for modulating the Zn^{2+} storage capability of MnO, intrinsic regulation of lattice could be especially effective for improving the electrochemical performance, owing to the fundamental structure–property relationship.[14] Herein, we dope anionic sulphur into the lattice of MnO ($MnOS_x$) from Mn-based MOF to regulate the property of MnO, and further wrap $MnOS_x$ spheres outside by reduced graphene oxide (rGO) with good conductivity. Specifically, the doping of S intrinsically contributes more density of states (DOS) of electrons around the Fermi level, which promotes the electron transport. Moreover, sulphur doping-induced lattice expansion boosts the zinc-ion insertion/extraction kinetics. These two factors lead to improved rate performance and long-term reversible capacity. Therefore, when used as a cathode in ZIBs, $MnOS_{0.3}$@rGO exhibits a reversible specific capacity of 115.1 mA h g^{-1} after 350 cycles at a high rate of 0.5 A g^{-1}, much better than the pristine MnO. This enhanced performance demonstrates the potential of $MnOS_{0.3}$@rGO as a cathode material for ZIBs.[15]

A typical synthesis of $MnOS_{0.3}$@rGO is schematically illustrated in Fig. 1a. Namely, a certain amount of graphene oxide (GO) was added into the solution containing manganese acetate, polyvinyl pyrrolidone (PVP) and 1,3,5-benzenetricarboxylic (BTC) acid. After reaction for 24 hours at 60 °C, the product (Mn-BTC MOF) was formed. Subsequently, Mn-BTC@GO was annealed at 700 °C in an argon atmosphere for 3 hours at a heating rate of 5 °C min^{-1} to obtain MnO@rGO. Then a certain amount of sulphur powder was mixed with MnO@rGO and underwent secondary annealing at 400 °C in an argon atmosphere for 2 hours at a heating rate of 5 °C min^{-1} to obtain $MnOS_{0.3}$@rGO. The control samples, such as pristine MnO and $MnOS_{0.3}$ were also synthesized by using the similar method, except the addition of sulphur powder and/or GO.

[a] *School of Materials Science and Engineering, Suzhou University of Science and Technology, Suzhou 215009, China. E-mail: ruguangma@usts.edu.cn*
[b] *Research Unit of Sustainable Chemistry, University of Oulu, Oulu 90570, Finland. E-mail: ulla.lassi@oulu.fi*
[c] *School of Chemistry and Materials Engineering, New Energy Materials and Technology Research Centre, Huainan Normal University, Huainan 232038, Anhui, China*

† Electronic supplementary information (ESI) available. See DOI: https://doi.org/10.1039/d4cc04773g

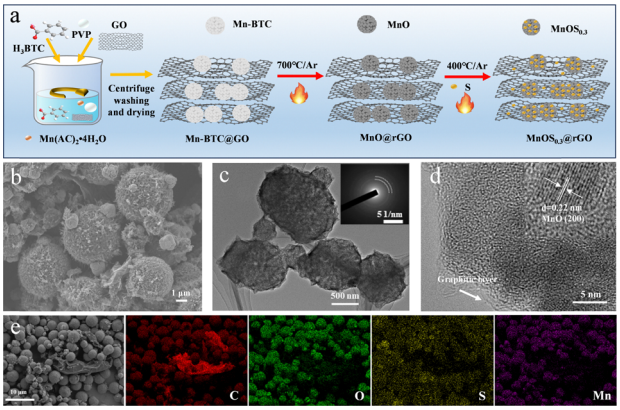

Fig. 1 (a) Scheme of synthetic process of $MnOS_{0.3}$@rGO. (b) SEM image, (c) TEM image and SAED image (inset), (d) HRTEM image with clear lattice fringes (inset), and (e) EDS and element mapping images of $MnOS_{0.3}$@rGO.

Scanning electron microscopy (SEM) image shows that the morphology of $MnOS_{0.3}$@rGO is hierarchical spheres consisting of many nanoparticles (Fig. 1b and Fig. S1, ESI†). Transmission electron microscopy (TEM) clearly reveals that some nanospheres assigned to $MnOS_{0.3}$ are wrapped by rGO layers (Fig. 1c). The selected area electron diffraction (SAED) shows concentric rings, indicating the polycrystallinity of $MnOS_{0.3}$ nanoparticle (inset of Fig. 1c). The enlarged TEM image shows that a typical nanoparticle with the size of 8 nm is wrapped by a few graphitic layers. Such microstructure is beneficial for the improvement of electrical conductivity. High-resolution TEM (HRTEM) image (inset of Fig. 1d) shows obvious lattice fringes, which also demonstrates the good crystallinity of $MnOS_{0.3}$. The lattice spacing is 0.22 nm, corresponding to the (200) facet of MnO. Energy-dispersive X-ray spectroscopy (EDS) image (Fig. 1e) and the corresponding elemental mapping images, reveal the existence of Mn, S, C and O elements uniformly distributing throughout the entire $MnOS_{0.3}$@rGO. SEM image and the corresponding elemental mapping images of $MnOS_{0.3}$ also confirm the uniform distribution (Fig. S2 in ESI†).

X-ray diffraction (XRD) patterns as shown in Fig. 2a and Fig. S3 (ESI†), clearly show the crystal structure of $MnOS_{0.3}$@rGO, which match well with MnO (JCPDS no. 07-0230), confirming the successful synthesis. Compared to the pattern of pristine MnO, the peaks of $MnOS_{0.3}$ and $MnOS_{0.3}$@rGO show a little shift toward low angle due to S doping, especially for the peaks corresponding to (200) and (220). In Raman spectra (Fig. 2b), the typical peak at 646.5 cm^{-1} is ascribed to Mn–O vibration, which also indicates the formation of MnO.[16] Two prominent peaks at 1342 and 1591 cm^{-1} are assigned to the D band and G band, respectively, which is caused by the rGO and carbonization of Mn-BTC. The intensity ratio (I_D/I_G) of $MnOS_{0.3}$@rGO is about 0.95, which is a little lower than that of MnO (1.07). This could be caused by the good graphitization of rGO, which is beneficial for the electrical conductivity.[17]

To analyse the surface chemical state of different elements in $MnOS_{0.3}$@rGO, X-ray photoemission spectroscopy (XPS) was conducted. The peaks in the C 1s XPS spectrum (Fig. 2c) located at 284.3, 288.6, and 285.4 eV, correspond to C–C, C═O, and

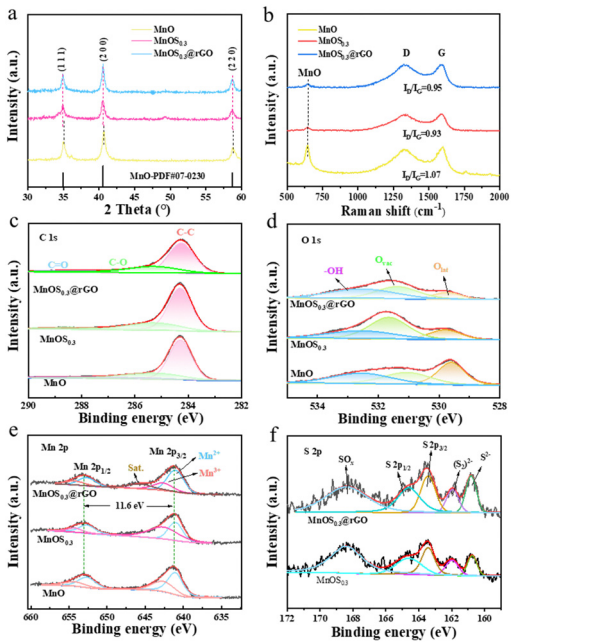

Fig. 2 (a) XRD patterns, (b) Raman spectra, (c) C 1s XPS spectra, (d) O 1s XPS spectra; (e) Mn 2p XPS spectra of MnO, $MnOS_{0.3}$, and $MnOS_{0.3}$@rGO; and (f) S 2p XPS spectra $MnOS_{0.3}$, and $MnOS_{0.3}$@rGO.

C–O bonds, respectively. The peaks in the O 1s spectrum (Fig. 2d) located at 529.8, 531.4, and 532.8 eV, correspond to O_{lat} (Mn–O), O_{vac}, and –OH bonds, respectively. The relative intensity of O_{vac} peak to O_{lat} peak increases in both $MnOS_{0.3}$ and $MnOS_{0.3}$@rGO can be attributed to the reaction between O in MnO and carbon derived from MOF at the high temperature. In addition, the addition of rGO also affects the intensity of O 1s peaks due to the interaction between residual oxygen-containing functional groups and $MnOS_{0.3}$. The Mn 2p spectrum shows two main peaks at about 641.3 and 652.9 eV (Fig. 2e), corresponding to Mn $2p_{1/2}$ and Mn $2p_{3/2}$, respectively.[18] The spin energy separation is 11.6 eV, which is typical of MnO phase.[19] The S 2p XPS spectrum shows five main peaks of SO_x, S $2p_{1/2}$, S $2p_{3/2}$, $(S_2)^{2-}$, and S^{2-} located at 168.3, 161.9, 163.4, 164.6, and 160.9 eV (Fig. 2f), respectively, indicating the presence of S–O and S–Mn bonds.[15,20] The nitrogen sorption isotherm shows (Fig. S4a, ESI†) that the Brunauer–Emmett–Teller (BET) specific surface area of $MnOS_{0.3}$@rGO is 82.6 $m^2\ g^{-1}$, much lower than that of MnO (235.8 $m^2\ g^{-1}$) and $MnOS_{0.3}$ (115.6 $m^2\ g^{-1}$). But $MnOS_{0.3}$@rGO shows abundant micropores (Fig. S4b, ESI†) rather than mesopores compared to MnO and $MnOS_{0.3}$, which provide rapid transport channels for the storage of H^+ and Zn^{2+}, thus remarkably facilitating the diffusion kinetics of guest ions. The carbon content of MnO, $MnOS_{0.3}$ and $MnOS_{0.3}$@rGO was analysed through the thermal gravimetric analysis (TGA) as shown in Fig. S5 (ESI†). The mass loss before 200 °C is attributed to the reduction of crystal water. The subsequent mass decrease after 200 °C is caused by the loss of carbon. Based on the TGA curve, the calculated carbon content of MnO, $MnOS_{0.3}$ and $MnOS_{0.3}$@rGO in the material is about 24.57%, 18.99%, and 20.17%, respectively.

The electrochemical performance of $MnOS_{0.3}$@rGO material as a cathode for ZIBs was evaluated in a half cell by using zinc foil

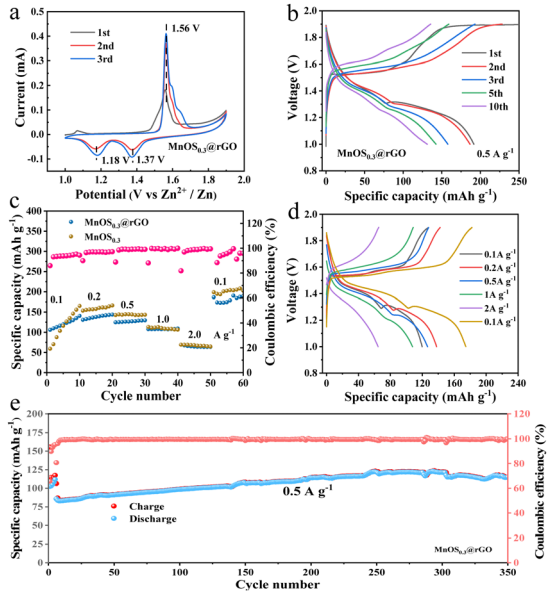

Fig. 3 (a) CV curves of $MnOS_{0.3}$@rGO at a scanning rate of 0.1 mV s^{-1}; (b) charging and discharging curves of different cycle number at a current density of 0.5 A g^{-1}; (c) rate capabilities; (d) charge/discharge curves of $MnOS_{0.3}$@rGO at different current densities; and (e) cycling performance at 0.5 A g^{-1} for the $MnOS_{0.3}$@rGO electrodes.

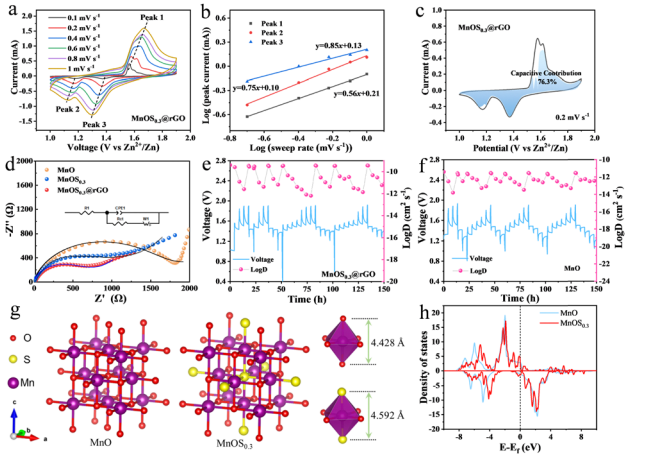

Fig. 4 (a) CV curves measured at different scan rates from 0.2 to 0.8 mV s^{-1}; (b) *b* value according to the relationship of log(*i*) and log(*v*) at different peaks; (c) pseudocapacitive contributions (shaded area) at a scan rate of 0.2 mV s^{-1}; (d) EIS of the MnO, $MnOS_{0.3}$, and $MnOS_{0.3}$@rGO; (e) and (f) charge/discharge profiles of $MnOS_{0.3}$@rGO electrode in GITT test and the Zn^{2+} diffusivity coefficient; (g) structure model and (h) projected DOS of MnO, and $MnOS_{0.3}$.

as anode. The cyclic voltammetry (CV) curves of MnO, $MnOS_{0.3}$, and $MnOS_{0.3}$@rGO at 0.1 mV s^{-1} are shown in Fig. 3a and Fig. S6 (ESI†). They show the similar redox peaks due to the same reaction mechanism. But the positions of redox peaks show a little difference. $MnOS_{0.3}$@rGO shows two cathodic peaks at 1.37 and 1.18 V, corresponding to H^+ insertion and Zn^{2+} insertion, respectively. The cathodic reduction peak of $MnOS_{0.3}$ shifts slightly to the high potential (*i.e.*, 1.21 V). In addition, $MnOS_{0.3}$ and $MnOS_{0.3}$@rGO show similar curve areas, much larger than the area of MnO, indicating the improved capacity. Fig. 3b shows the capacity of $MnOS_{0.3}$@rGO after different cycles. Two plateaus become remarkable during the discharge/charge process, which corresponds to intercalation/deintercalation of H^+ and Zn^{2+}, respectively.[21] Fig. 3c shows the rate performance of $MnOS_{0.3}$@rGO at different current densities. The reversible capacity is about 165.3, 144, 129.7, 109.2, and 64.6 mA h g^{-1} at 0.1, 0.2, 0.5, 1.0, and 2.0 A g^{-1}, respectively, much higher than that of MnO (40.7, 36.9, 45.2, 45, and 40.6 mA h g^{-1}). Fig. 3d shows the charge–discharge curves of $MnOS_{0.3}$@rGO at 0.1, 0.2, 0.5, 1.0, and 2.0 A g^{-1}. At the current density higher than 0.2 A g^{-1}, the capacity approaches to be stable, indicating good reaction kinetics. In addition, when the current returns to 0.1 A g^{-1}, the capacity increases compared to the initial value, which is caused by the activation required by the electrode material itself. The enhanced electrochemical performance of $MnOS_{0.3}$@rGO can be attributed to the excellent conductivity of rGO and graphitic layer, which enables higher electrochemical activity and faster electron/ion diffusion in the cathode.

Fig. 3e shows the cycling performance of $MnOS_{0.3}$@rGO at 0.5 A g^{-1} after five-cycle activation at 0.1 A g^{-1}. It can be seen that $MnOS_{0.3}$@rGO initially exhibits the capacity of about 85.8 mA h g^{-1}. With the increase of cycling number, the capacity gradually increases up to 100.6 mA h g^{-1}, much higher than that of $MnOS_{0.3}$ (Fig. S7, ESI†). The initial increase of specific capacity could be attributed to an electrochemical activation process. In this process, incomplete deintercalated zinc ions act as "pillars" between layers to improve the structural stability and contribute to the enhanced capacity.[22] After activation, the specific capacity of about 115.1 mA h g^{-1} remains relatively stable over 350 cycles. In addition, the Coulombic efficiency of $MnOS_{0.3}$@rGO almost keeps 100% at 0.5 A g^{-1}, demonstrating good reversibility. The more stable cycle performance and higher capacity of $MnOS_{0.3}$@rGO, could be attributed to the synergistic effect of S doping and rGO.

In order to further understand the advantages of S doping and rGO wrap, the electrochemical reaction kinetics was analyzed based on CV curves at different scanning rates (0.1–1 mV s^{-1}) in Fig. 4a. The CV curves illustrate similar shapes and peaks at different scanning rates. The CV curve can be divided into diffusion-controlled and capacitive processes. And the measured peak current (*i*) and scanning rate (*v*) follow eqn (1) and (2):[23]

$$i = av^b \quad (1)$$

$$\log(i) = b\log(v) + \log(a) \quad (2)$$

where the *b* value close to 1 indicates that the capacity of the material is controlled by the capacitive process, while a value close to 0.5 indicates the diffusion-controlled process. As shown in Fig. 4b, the *b* value of $MnOS_{0.3}$@rGO indicates that the capacity of $MnOS_{0.3}$@rGO is controlled by diffusion and surface capacitance processes.

$$i(\nu) = k_1\nu + k_2^{\frac{1}{2}} \quad (3)$$

The ratio of capacitance to diffusion-controlled capacity can be quantified using eqn (3), where $i(\nu)$, $k_1\nu$, and $k_2^{\frac{1}{2}}$ correspond

to the measured current, the current contributed by the capacitance, and the current contributed by diffusion-controlled process, respectively.[24] As shown in Fig. 4c and Fig. S8 and S9 (ESI†), the capacitance contribution of $MnOS_{0.3}$@rGO electrode at the scanning rate of 0.2, 0.4, 0.6 and 0.8 mV s^{-1} is 79.3%, 79.5%, 79.6% and 79.2%, which is higher than the corresponding value of MnO. Due to S doping, the diffusion efficiency is improved, which is conducive to the transport of Zn^{2+} ions and electrons during the insertion/extraction process. Fig. 4d shows the electrochemical impedance spectroscopy (EIS) results of MnO, $MnOS_{0.3}$, and $MnOS_{0.3}$@rGO. Nyquist plot of each sample shows a typical semicircle, corresponding to the charge-transfer resistance (R_{ct}) in the high-frequency region. Compared to MnO and $MnOS_{0.3}$, $MnOS_{0.3}$@rGO has the smallest radius, with an R_{ct} of about 728.4 Ω, much lower than that of MnO (1559 Ω) and $MnOS_{0.3}$ (917 Ω).

Galvanostatic intermittent titration technique (GITT) was also employed to measure the diffusion coefficient of Zn^{2+} ($D_{Zn^{2+}}$) according to eqn (4):[25]

$$D_{Zn^{2+}} = \frac{4}{\pi\tau}\left(\frac{n_M V_M}{s}\right)^2\left(\frac{\Delta E_s}{\Delta E_\tau}\right)^2 \quad (4)$$

where n_M and V_M are the molar mass and molar volume of the samples, respectively, S stands for the active surface area of the electrode, t is the relaxation time, and ΔE_s and ΔE_τ represent the potential change between steps and during the current pulse, respectively. Under different charging and discharging states (Fig. 4e and f), the $D_{Zn^{2+}}$ (10^{-12}–10^{-9} cm^2 s^{-1}) of $MnOS_{0.3}$@rGO is relatively larger than that of $MnOS_{0.3}$ (10^{-14}–10^{-12} cm^2 s^{-1}) and MnO (10^{-13}–10^{-12} cm^2 s^{-1}), which means that S doping and rGO wrap accelerate the diffusion kinetics.

To gain insights into the underlying mechanism, density functional theory (DFT) calculations were conducted by constructing MnO and S-doped MnO models (Fig. 4g). After the construction optimization, it is found the lattice constant is expanded from 4.428 to 4.592 Å, which is consistent with the low-angle shift of XRD peaks. The expanded lattice with large pathway for the Zn^{2+} diffusion endows $MnOS_{0.3}$ with good rate performance. The projected density of states (DOS) of electrons in Fig. 4h increases around Fermi level after S doping, which suggests that the substitution of O atom with S atom improves the electrical conductivity of MnO. Coupling with the external rGO wrap, $MnOS_{0.3}$@rGO demonstrates good cycling stability and rate capability.

In conclusion, $MnOS_{0.3}$@rGO has been successfully synthesized by doping S into MnO@rGO at high temperature. S doping into MnO expands the lattice of MnO, providing larger pathways for ion transport, while the increased DOS around Fermi level improves the electrical conductivity of $MnOS_{0.3}$, boosting the electron transport. The synergistical improvement of ion/electron transport effectively lowers the Zn^{2+} diffusion barrier, enabling faster Zn^{2+} insertion/extraction kinetics. Coupling the external rGO wrap, $MnOS_{0.3}$@rGO demonstrates superior Zn^{2+} storage capability and good rate performance in ZIBs. This work opens a new avenue for the development of next-generation aqueous ZIBs.

Z. C. and L. S. carried out the synthesis and characterization. Y. L., S. Y., Z. W. and T. H. performed partial characterization. U. L. and R. M. supervised the project. All authors contributed to writing the manuscript.

This work was supported by the National Natural Science Foundation of China (No. 52172058). Yan Lin, Tao Hu and Ulla Lassi acknowledge Business Finland for research funding (BATCircle2.0, 44612/31/2020).

Data availability

The data that supports the findings of this study are available in the manuscript and ESI† of this article.

Conflicts of interest

There are no conflicts to declare.

Notes and references

1 Z. Azmi, K. C. Senapati, A. K. Goswami and S. R. Mohapatra, *J. Power Sources*, 2024, **613**, 234816.
2 X. Guo, C. Li, X. Wang, Z. Li, H. Zeng, P. Hou, M. Xie, Y. Li, Z. Shi and S. Feng, *Sci. China Chem.*, 2023, **66**, 1406–1416.
3 Y. Zhang, J. Liang, M. Wu, Q. Tang, Y. Xie, Z. Li, S. Lu, L. Qin and X. Fan, *Mater. Today Commun.*, 2024, **39**, 108942.
4 Z.-X. Zhu, Z.-W. Lin, Z.-W. Sun, P.-X. Zhang, C.-P. Li, R. Dong and H.-W. Mi, *Rare Met.*, 2022, **41**, 3729–3739.
5 H. Zhang, Z. Shen, D. Jia, W. Zhou, X. Wang, J. Liu and X. He, *J. Alloys Compd.*, 2024, **991**, 174413.
6 A. Zhang, X. Zhang, H. Zhao, H. Ehrenberg, G. Chen, I. Saadoune, Q. Fu, Y. Wei and Y. Wang, *J. Colloid Interface Sci.*, 2024, **669**, 723–730.
7 Q. Shi, R. Mu, W. Zhang, C. Zhang, Z. Chang, Q. Cui, B. Wang and D. Gu, *J. Energy Storage*, 2024, **96**, 112662.
8 S. H. Luo, X. Meng, K. Cai, H. Chen, L. Qian, J. Guo, S.-X. Yan, Q. Wang, X. Ji and X. Zhou, *J. Power Sources*, 2024, **603**, 234485.
9 S. Gong, J. Zhao, K. Sun, X. Jia and D. Chao, *Appl. Energy*, 2024, **365**, 123284.
10 X. Xiao, T. Wang, Y. Zhao, W. Gao and S. Wang, *J. Colloid Interface Sci.*, 2023, **642**, 340–350.
11 Y. Liu, Y. Ma, W. Yang, S. Bao, H. Chen and M. Xu, *Chem. Eng. J.*, 2023, **473**, 145490.
12 F. Tang, J. Gao, Q. Ruan, X. Wu, X. Wu, T. Zhang, Z. Liu, Y. Xiang, Z. He and X. Wu, *Electrochim. Acta*, 2020, **353**, 136570.
13 X. Mao, X. Zhang, Y. Zeng, A. F. Halima and P. K. Shen, *Energy Technol.*, 2021, **9**, 2100022.
14 Q. Dai, L. Li, T. Tu, M. Zhang and L. Song, *J. Mater. Chem. A*, 2022, **10**, 23722–23730.
15 S. Xu, S. Fan, W. Ma, J. Fan and G. Li, *Inorg. Chem. Front.*, 2022, **9**, 1481–1489.
16 Y. Chen, X. Hu, X. Chen, J.-H. Liu, Y. Huang and D. Cao, *Chem. Eng. J.*, 2023, **478**, 147411.
17 Z. Liu, Z. Qiu, Z. Li, T. Wei, Z. Fan and H. Pang, *Sci. China Chem.*, 2024, **67**, 2930–2940.
18 L. Li, Y. Wang, G. Jiang, J. Li, M. Wang, Y. Niu and E. Shangguan, *Mater. Chem. Front.*, 2022, **6**, 3193–3204.
19 X. Li, Q. Liu, X. Ma, P. Liu, D. Wang, X. Yu and Y. Liu, *J. Mater. Chem. A*, 2023, **11**, 19566–19577.
20 F. Tang, X. Wu, Y. Shen, Y. Xiang, X. Wu, L. Xiong and X. Wu, *Energy Storage Mater.*, 2022, **52**, 180–188.
21 L. Yan, B. Liu, J. Hao, Y. Han, C. Zhu, F. Liu, X. Zou, Y. Zhou and B. Xiang, *J. Energy Chem.*, 2023, **82**, 88–102.
22 Q. Zong, W. Du, C. Liu, H. Yang, Q. Zhang, Z. Zhou, M. Atif, M. Alsalhi and G. Cao, *Nano-Micro Lett.*, 2021, **13**, 116.
23 H. Zhang, Y. Zhang, X. Li, J. Zhang, Y. He, X. Yang, J. Xu, D. Jia and J. Liu, *J. Energy Storage*, 2024, **87**, 111331.
24 X. Yu, D. Yu, Y. Li, H. Niu, T. Zhang, W. Yang and D. Sun, *J. Energy Storage*, 2024, **93**, 112456.
25 H. Xu, M. Li, P. Guo, W. Yang, C. Li, H. Wang, W. Peng and L. Jiapeng, *Carbon*, 2024, **228**, 119403.

